Advanced Engineering Materials

ADVANCED ENGINEERING MATERIALS
www.aem-journal.com

RESEARCH ARTICLE

From Shear to Sound: Mechanics–Acoustics Mapping of TPMS Lattices

Lucía Doyle[1,2] | María Ángeles Navacerrada[3] | Johan Christensen[1] | Carlos González[1,4]

[1]IMDEA Materials, Getafe, Madrid, Spain | [2]Universidad Alfonso X el Sabio, Villanueva de la Cañada, Madrid, Spain | [3]Universidad Politécnica de Madrid, E.T.S. de Arquitectura, Madrid, Spain | [4]Departamento de Ciencia de Materiales, Universidad Politécnica de Madrid, E.T.S. de Ingenieros de Caminos, Madrid, Spain

Correspondence: Lucía Doyle (luciadoyle@uax.es)

Received: 2 February 2026 | **Revised:** 16 April 2026 | **Accepted:** 12 May 2026

Keywords: bulk | cellular solids | mechanics | property space | shear | sound absorption | topology | TPMS

ABSTRACT

Triply periodic minimal surface (TPMS) lattices offer a framework for integrating load-bearing capacity and functional response within a single architected material. However, existing studies have largely focused on compression and treated mechanical and acoustic properties independently. Here, we map the coupled mechanical and acoustic performance of TPMS architectures across relative densities of 15%–75%, combining simulations and experiments, including a dedicated shear testing methodology. We show that commonly used descriptors, including Gibson–Ashby scaling and load-aligned solid fraction, fail to predict shear and bulk stiffness, despite their proven validity for the same TPMS under compression. This reveals a fundamental limitation of existing models when extended to shear, where stiffness is governed by connectivity, cross-sectional heterogeneity, and complex strain distribution pathways that are not captured by either the Gibson–Ashby scaling or the load-aligned solid fraction. Acoustically, a transition occurs at 25% relative density: below this threshold, all architectures exhibit broadband absorption governed by viscothermal losses, whereas at higher densities, constrictions generate coupled neck–cavity elements that induce distributed resonance. The peak absorption scales with cavity-to-neck ratio. Density grading tunes absorption while preserving overall mass and thickness. These results establish TPMS lattices as a platform for multifunctional, load-bearing acoustic materials.

1 | Introduction

Modern engineering systems increasingly demand materials that do more than carry load. In applications ranging from transportation and aerospace to building technologies and industrial equipment, structural components are often required to simultaneously provide mechanical stiffness, stability under complex loading, and effective control of noise and vibration. Traditionally, these functions are achieved by combining separate materials or adding auxiliary layers, leading to increased weight, complexity, and manufacturing cost. Architected metamaterials and metamaterials offer an alternative approach, enabling mechanical and acoustic functionalities to be embedded directly into the material architecture itself [1–4]. In this context, triply periodic minimal surface (TPMS) lattices have emerged as promising candidates, as their continuous and interconnected geometry naturally couples structural integrity with the ability to manipulate sound through controlled porosity and internal cavities.

TPMS are surfaces in $\mathbb{R}^3$ which have the necessary condition to have zero mean curvature. They repeat infinitely in the three directions, filling up space, and dividing it into two geometrically disconnected labyrinthine domains, thus also termed space partitioners [5]. TPMS can be represented as periodic nodal or zero-level potential surfaces and are commonly described using a level-set function $\phi(x, y, z) = t$ [6–8], allowing for the generation of 3D structures. One approach, followed in the present work, is to to define the region occupied by the solid phase, for instance,

© 2026 Wiley-VCH GmbH.

as negative, $\phi(x, y, z) - t < 0$, or as positive, $\phi(x, y, z) - t > 0$. Lattices obtained following this methodology can be found termed strut-based, network-based, skeletal solid, or tubular [9]. Combining the positive and negative lattices results in a solid cube, for TPMS of cubic symmetry. An alternative approach to generate 3D lattices is to thicken the surface into solid walls by offsetting it on both sides by a distance t, expressed as $(\phi - t)(\phi + t) < 0$. TPMS lattices produced this way are commonly referred to as sheet, shell, double, or walled [9]. Each structure exists only within a specific t range; outside this interval, one phase breaks into disconnected regions (pinch-off), defining the achievable relative density range. The cross-sectional variability of lattice members strongly influences this range, with important implications for mechanical and functional performance.

Despite growing interest in TPMS lattices and their recognized multifunctional potential [10], studies to date remain scattered. Mechanically, most work has examined only the compressive response of a few architectures [11–17], with shear and bulk behavior largely unexplored.

Functional studies, such as sound absorption [18, 19], phononic bandgaps [20, 21], or flow resistivity [22], have been limited to only two or three architectures and primarily focused on characterization, providing little insight into structure–property relationships. Our recent study began to address this gap by reporting uniaxial compression for 36 architectures [23], providing the most extensive mechanical dataset to date. Yet, a comprehensive, systematic mapping of mechanical and acoustic behavior across architectures and relative densities is still lacking. The present work fills this gap by combining shear, bulk, and acoustic characterization, revealing the multifunctional design space of TPMS and highlighting how architecture and material distribution govern performance. A key methodological advance is the experimental determination of lattice shear response, for which no prior experimental studies have been identified, providing both a validation of numerical predictions and a new testing framework. The results reveal a rich diversity of strain transmission pathways across TPMS topologies and demonstrate that shear and bulk stiffness emerge from a complex interplay of cross-sectional variations, connectivity, and load-aligned solid fraction (LASF).

From an acoustic perspective, our results reveal a clear transition in behavior with relative density. At low relative densities (below ~25%), all TPMS architectures exhibit nearly identical absorption frequencies, indicating that the acoustic response is dominated by porosity rather than specific geometry. This challenges the common assumption that different lattice families must be treated as fundamentally distinct. As density increases, resonance effects emerge, influenced by the ratio of cavity to neck and by flow resistivity, highlighting the role of architecture. Importantly, we demonstrate that density grading provides a practical means to optimize acoustic performance independently of structural weight, especially for architectures with low pinch-off.

Together with the mechanical characterization, these findings highlight that the true advantage of TPMS lies in their multifunctional potential: by selecting architectures and relative densities across the mapped property space, and applying strategies such as density grading, engineers can tailor both mechanical performance under multiaxial loads and acoustic absorption, unlocking combinations of properties that single-purpose truss lattices cannot provide.

2 | Results

2.1 | Shear and Bulk Mechanics of TPMS Architectures: From Simulation to Experimental Validation

The shear and bulk behavior of 36 TPMS-based lattices was studied through numerical simulations, in the relative density range spanning from the pinch-off point of each architecture up to 60% relative density in 5% intervals. The implicit equations of all studied architectures can be found in our previous work [23]. The list of pinch-off relative densities for all studied architectures can be found in the Supporting Information, Section 0.1. The extensive dataset of bulk and shear moduli generated in this work, together with our previously reported Young's modulus values for the same TPMS architectures [23], enables the construction of comprehensive mechanical property maps, as shown in Figure 1. Truss lattices BCC, FCC, and octet have been additionally simulated and included for comparison.

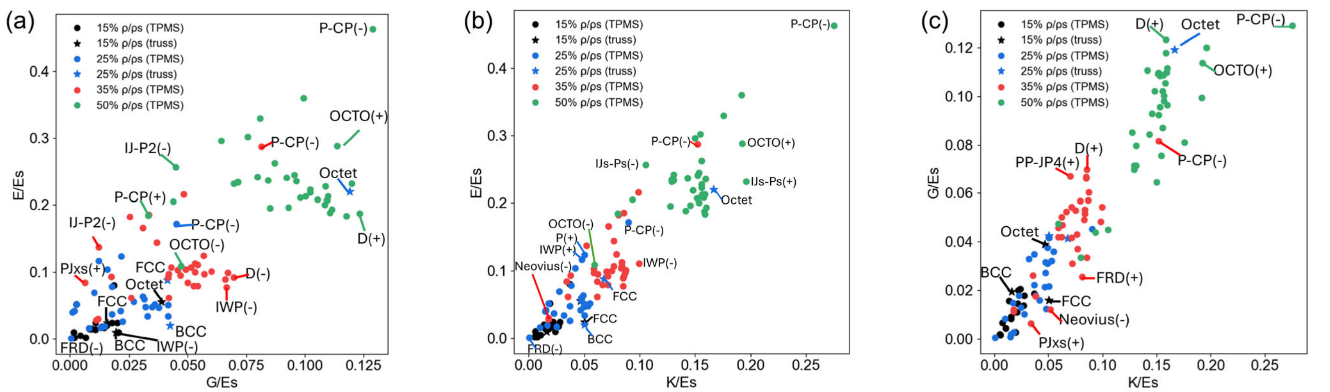

FIGURE 1 | Normalized moduli of TPMS strut-based lattices at different relative densities illustrating the mechanical design space spanned by these architectures. Panels show (a) E/E_s versus G/G_s, (b) E/E_s versus K/K_s, and (c) G/G_s versus K/K_s. Truss lattices BCC, FCC, and octet are included for reference. For readability, only selected data points corresponding to extrema and representative architectures are labeled. The complete dataset is provided in Tables S2–S6, Supporting Information, Section 0.2.

15272648, 2026, 14, Downloaded from https://advanced.onlinelibrary.wiley.com/doi/10.1002/adem.70951 by Spanish Cochrane National Provision (Ministerio de Sanidad), Wiley Online Library on [24/07/2026]. See the Terms and Conditions (https://onlinelibrary.wiley.com/terms-and-conditions) on Wiley Online Library for rules of use; OA articles are governed by the applicable Creative Commons License

All plotted data are tabulated in the Supporting Information, Section 0.2, for full accessibility. Further, complete moduli–relative density plots for all investigated architectures are included in the Supporting Information, Section 0.3.

It can be seen that the TPMS span a wide range of elastic moduli and intermodulus relationships (E–G, E–K, G–K) across the studied relative densities, delineating a broad mechanical design space. To contextualize this space, reference truss lattices (BCC, FCC, and octet) are included, enabling direct comparison across fundamentally different architectural families.

The combined dataset enables, for the first time to our knowledge, a direct mapping of TPMS architectures together with classical truss lattices within a unified mechanical property space. This representation reveals not only the wide span of elastic responses achievable with TPMS but also their relative positioning within the broader mechanical landscape. In this context, the truss lattices serve not as direct competitors but as reference structures that help interpret the distribution of TPMS architectures across the design space.

Within this unified representation, the comparatively high stiffness of the octet lattice at low relative density reflects its well-known stretch-dominated and kinematically rigid behavior and should not be interpreted as anomalous. Rather, it defines an upper-bound reference for stiffness efficiency, against which the broader distribution of TPMS architectures can be interpreted. In contrast, TPMS architectures occupy a wider and more continuous region of the design space, reflecting their distributed geometry and more complex deformation pathways.

In order to validate the numerical simulations, experimental shear tests were conducted. Given the lack of standards or work concerning experimental shear tests of lattices in general, we here propose an adaptation of the ASTM D7078 test method Shear Properties of Composite Materials [24]. Samples were designed to have four unit cells along the length of the specimen and two unit cells through the thickness to allow for three-dimensional continuity of the lattice while maintaining sufficient gauge volume for strain measurement and still fitting within the grips of the test machine. Additionally, the V-notch was centered within the middle unit cell rather than at the junction between two cells, in order to ensure that the local stress and strain fields in the gauge region were consistent with those in the corresponding numerical model (single unit cell with periodic boundary conditions). The obtained stress–strain curves (experimental and by finite element modeling [FEM]) are presented in Figure 2.

Digital image correlation (DIC) was performed from image-based tracking during the tests. Figure 3 presents the in-plane shear strain distribution at the onset of yielding for the tested architectures, all at a comparable relative density of $\sim$30% ρ/ρ_s, to highlight the influence of architecture on the deformation patterns.

While DIC measurements inherently exhibit a certain level of spatial noise and do not provide the same visual sharpness as idealized numerical simulations, they offer direct experimental

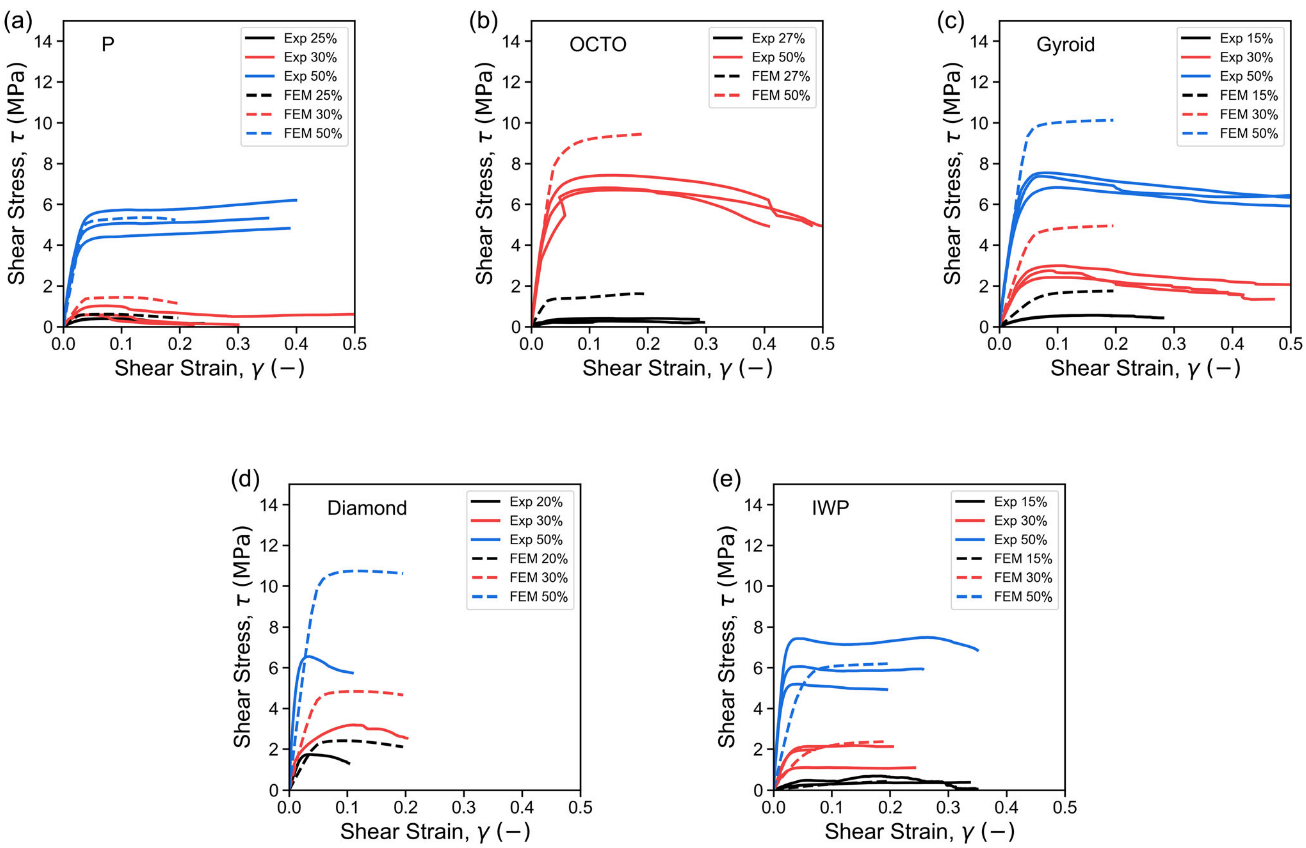

FIGURE 2 | Shear stress–strain curves from experimental tests and numerical simulations at different relative densities for (a) P (+), (b) OCTO (+), (c) Gyroid (+), (d) D (+), and (e) IWP (+).

15272648, 2026, 14, Downloaded from https://advanced.onlinelibrary.wiley.com/doi/10.1002/adem.70951 by Spanish Cochrane National Provision (Ministerio de Sanidad), Wiley Online Library on [24/07/2026]. See the Terms and Conditions (https://onlinelibrary.wiley.com/terms-and-conditions) on Wiley Online Library for rules of use; OA articles are governed by the applicable Creative Commons License

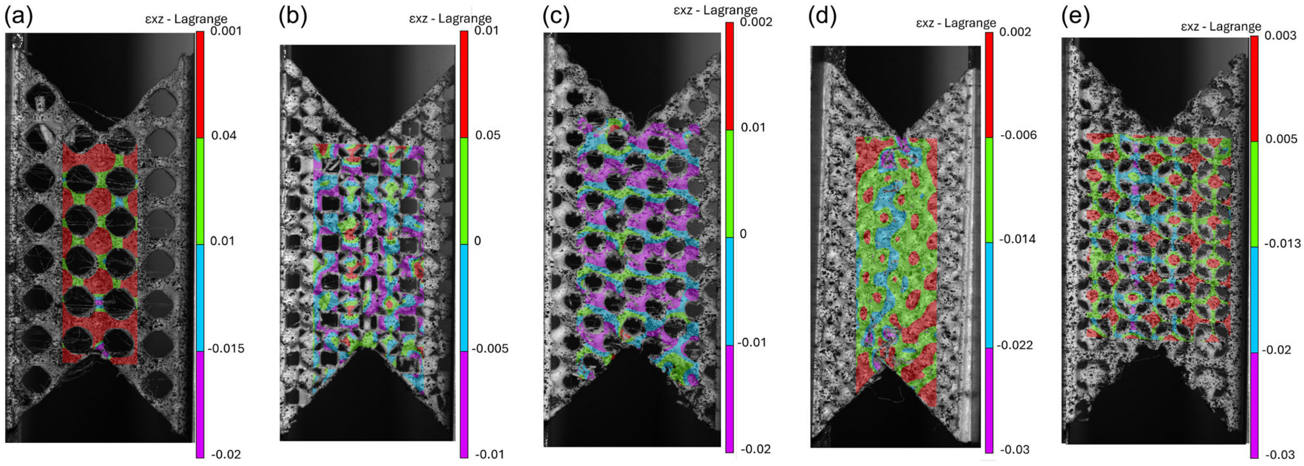

FIGURE 3 | Shear strain distribution at yield point for the tested TPMS with ∼30% ρ/ρ_s: (a) P (+), (b) OCTO (+), (c) Gyroid (+), (d) D (+), and (e) IWP (+).

insight into the strain localization mechanisms. Distinct shear patterns can nevertheless be identified across lattice types.

Architectures with relatively homogeneous strut thicknesses exhibit well-defined shear bands spanning the specimen (e.g., the Gyroid (+) in plot Figure 3c). In contrast, architectures with pronounced variations in strut thickness exhibit more fragmented strain localization patterns that follow local stiffness inhomogeneities (e.g., the P (+) in plot Figure 3a, OCTO (+) in plot Figure 3d, and IWP (+) in plot Figure 3e). For the Diamond (+) lattice (plot Figure 3d), the strain field reveals a pronounced localization along the line connecting the two notches, indicating a distinct shear response compared to the other geometries. These experimentally observed patterns are consistent with the expected influence of architectural connectivity and thickness distribution on shear deformation. Overall, the simulated and experimental stress–strain curves show good agreement in the elastic regime in terms of trend and order of magnitude. The FEA model captures the dependence of the shear modulus on relative density across all geometries, although some systematic deviations in magnitude are observed. The low variability observed across repeated measurements further supports the robustness and reproducibility of the proposed experimental methodology. It should be noted that the experimental stress state does not correspond to ideal pure shear. The double-notched specimen was designed following ASTM D7078, which is widely used to promote a shear-dominated stress state while reducing bending effects. However, stress gradients remain near the notch roots and free surfaces, and the stress state evolves with increasing deformation. In the present work, the geometry was adapted to lattice materials by embedding a periodic structure within the gauge section while maintaining solid gripping regions for proper load transfer. Although the initial response is predominantly shear-driven, local stress concentrations and geometric features of the lattice lead to deviations from ideal shear conditions. The experimentally measured yield point and subsequent plastic deformation are consistently lower than the numerical predictions. The reduced experimental yield strength may be influenced by both the nonideal stress state and the layered manufacturing process. Since the specimens were printed with layers stacked along the z-direction, the applied shear partly loads weaker interlayer interfaces rather than only the bulk material. These effects are not captured in the simulations and likely contribute to the earlier experimental yielding.

In order to study and derive structure–property relationships, the scaling relationship of G/E_s modulus and K/E_s with the relative density ρ/ρ_s for each architecture was studied by fitting the FEA data to the Gibson–Ashby power model for cellular solids [25]. Since the existence of TPMS-based network lattices does not start at relative density $\rho/\rho_s = 0$ but at their pinch-off relative density, the model was adjusted with a factor p (pinch-off) to include such effect, resulting in

$$\frac{G}{E_s} = \begin{cases} 0 & \frac{\rho}{\rho_s} < p \\ C_1\left(\frac{\rho}{\rho_s} - p\right)^n & \frac{\rho}{\rho_s} \geq p \end{cases} \tag{1}$$

and

$$\frac{K}{E_s} = \begin{cases} 0 & \frac{\rho}{\rho_s} < p \\ C_2\left(\frac{\rho}{\rho_s} - p\right)^m & \frac{\rho}{\rho_s} \geq p \end{cases} \tag{2}$$

where E_s stands for the elastic modulus of the solid material, ρ/ρ_s is the relative density of the lattice, and C_1, C_2 and n, m are fitting constants obtained by the least-squared method.

Additionally, the LASF, defined as the fraction of solid material aligned with the shear direction within the unit cell—corresponding to 45° relative to the x–y plane—was calculated using a ray-tracing routine implemented in Python.

Figure 4 presents the relationships between normalized shear modulus and Gibson–Ashby exponent (G vs. n) (plot a), normalized shear modulus and LASF (G vs. LASF) (plot b), and normalized bulk modulus and the corresponding Gibson–Ashby exponent (K vs. m) (plot c). These plots are shown for a relative density of 25%, where the TPMS struts can be more closely approximated as slender beams, in line with the assumptions underlying the Gibson–Ashby model. In addition, our previous analysis [23] has shown that both the fitted exponents and LASF exhibit the clearest and most meaningful trends at these lower relative densities.

The relationships shown in Figure 4 reveal several key trends that help interpret the mechanical behavior of the studied architectures. First, an overall inverse correlation between the Gibson–Ashby

15272648, 2026, 14, Downloaded from https://advanced.onlinelibrary.wiley.com/doi/10.1002/adem.70951 by Spanish Cochrane National Provision (Ministerio de Sanidad), Wiley Online Library on [24/07/2026]. See the Terms and Conditions (https://onlinelibrary.wiley.com/terms-and-conditions) on Wiley Online Library for rules of use; OA articles are governed by the applicable Creative Commons License

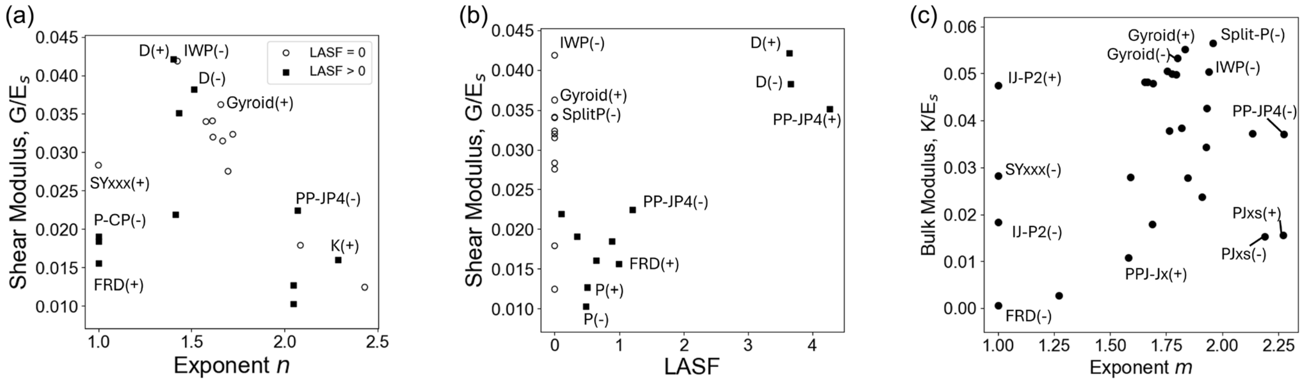

FIGURE 4 | (a) Relationships between normalized shear modulus and Gibson–Ashby exponent (G vs. n), (b) normalized shear modulus and LASF (G vs. LASF), and (c) normalized bulk modulus and the corresponding Gibson–Ashby exponent (K vs. m_K). Results are shown at a relative density of 25%. Open symbols denote architectures with zero LASF (LASF = 0), while filled symbols correspond to architectures with nonzero LASF.

exponent n and the normalized shear modulus G can be identified, although with some scatter, particularly for architectures with $n \approx 1$. Second, architectures with nonzero LASF generally exhibit higher shear stiffness; however, comparable values of G are also observed for structures with LASF = 0, indicating that LASF alone is not a sufficient descriptor. Finally, the fitted bulk modulus exponents deviate from the ideal value of $m = 1$, reflecting the influence of geometric heterogeneity and bending effects even in these periodic architectures.

In line with classical Gibson–Ashby arguments, plotting the fitted exponents against the normalized shear modulus reveals a clear inverse correlation between n and G: as n decreases, the shear stiffness generally increases, consistent with $n \approx 1$ reflecting stretch-dominated, rigid architectures and $n \approx 2$ corresponding to more bending-dominated, compliant behavior. Remarkably, however, the TPMS with $n = 1$ defy this expectation: rather than defining the upper envelope of shear stiffness, they span a wide range of G values, including comparatively modest ones. This unexpected behavior exposes the limits of the simple "lower $n \Rightarrow$ higher stiffness" paradigm and reveals a far richer, and still poorly understood, landscape for shear load transfer in lattice architectures than is typically assumed from axial loading alone.

Regarding the effect of LASF, we first note that only about half of the studied architectures exhibit any nonzero LASF at all. For those geometries that do have LASF, a higher LASF generally corresponds to a higher shear modulus G. However, architectures with zero LASF can still attain shear moduli comparable to, or even higher than, those of lattices with nonzero LASF. This indicates that shear stiffness is not governed by LASF alone, but is also strongly influenced by features such as the connectivity of the lattice members, the presence of larger contiguous solid regions, and variations in cross section.

For the bulk modulus, cubic lattices would be expected to exhibit a Gibson–Ashby exponent $m = 1$. In the ideal case of a perfectly isotropic cellular solid under purely hydrostatic loading, bending of the cell walls is suppressed and the bulk modulus scales linearly with relative density. However, as pointed out by Gibson and Ashby [25], imperfections such as nonuniformity in relative density or cell geometry promote bending and reduce the bulk stiffness below this ideal behavior. In our data, the fitted exponents m for the TPMS lattices deviate from the ideal value of 1, indicating that even these periodic architectures operate in a regime where geometric heterogeneity and local bending remain significant under nominally hydrostatic loading.

2.2 | From Mechanics to Sound: Acoustic Response of TPMS Architectures

To explore the acoustic performance across mechanically diverse TPMS, seven representative architectures were selected from the larger dataset.

The selection spans the full spectrum of elastic, shear, and bulk responses identified in the mechanical property maps and is further informed by previous studies on compression and low-velocity penetration [23, 26]. The selection includes structures maximizing shear and bulk moduli (D (+)), stiff lattices under compression (IWP (+)), compliant lattices (Gyroid (+), D (+), S (+), SYxxx (+)), and architectures with contrasting impact behavior, from resilient (IWP (+), Gyroid (+)) to highly energy-absorbing (OCTO (+)) lattices.

This selection enables a direct investigation of how distinct mechanical characteristics—such as stiffness, compliance, and energy absorption—translate into acoustic performance across different TPMS architectures. The sound absorption coefficients of the selected architectures were experimentally measured for a range of relative densities, starting from 15% up to 50%, depending on the pinch-off characteristics of each TPMS. Structures with higher pinch-off thresholds were thus tested from correspondingly higher starting relative densities. Samples with thicknesses between 1 and 4 cm, in 1 cm increments, were characterized. The resulting absorption curves for the frequency range of 1000–6500 Hz are shown in Figure 5, based on measurements performed with samples of 29 mm in diameter. Additional absorption curves for the lower frequency range of 500–1500 Hz, based on measurements performed with samples of 100 mm in diameter, are provided in the Supporting Information, Section 0.5, Figure S20.

The first observation is that, at low relative densities and low thicknesses, all lattices exhibit broadband sound absorption, characteristic of porous materials [27, 28], with generally low

15272648, 2026, 14, Downloaded from https://advanced.onlinelibrary.wiley.com/doi/10.1002/adem.70951 by Spanish Cochrane National Provision (Ministerio de Sanidad), Wiley Online Library on [24/07/2026]. See the Terms and Conditions (https://onlinelibrary.wiley.com/terms-and-conditions) on Wiley Online Library for rules of use; OA articles are governed by the applicable Creative Commons License

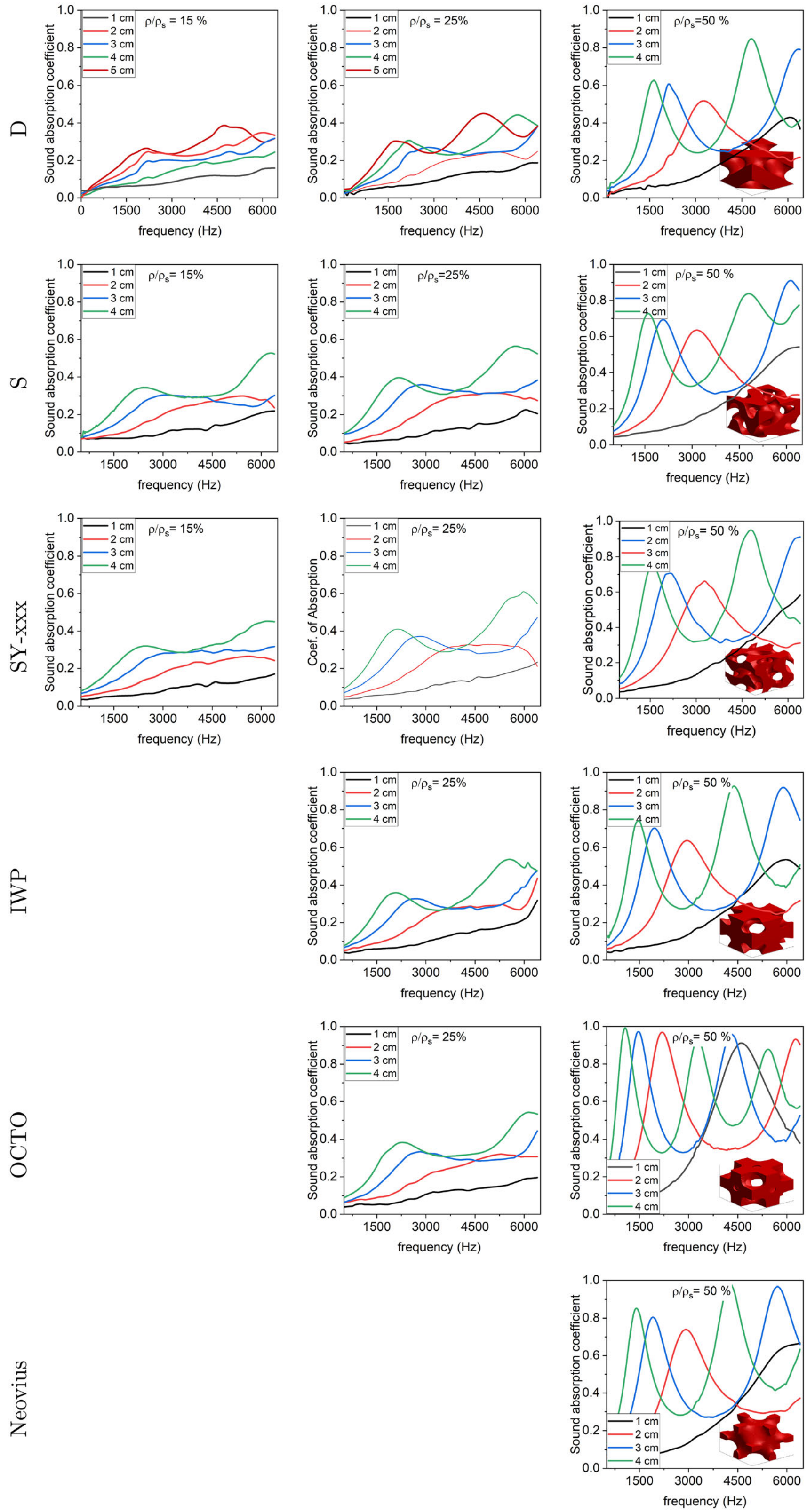

FIGURE 5 | Sound absorption curves for the studied lattice architectures. Rows indicate different architectures (labeled), and columns are arranged by increasing relative density from left to right.

absorption coefficients. As the relative density increases beyond approximately 25% and the thickness exceeds 2 cm, resonance effects become dominant, consistent with the transition from viscous–thermal dissipation toward a geometry-driven resonant response in structured porous materials [28].

A closer examination of the resonance regime reveals that, at a relative density of 25%, the position of the resonance peak is largely independent of architecture. In this regime, the response is primarily governed by the relative density, resulting in comparable resonance peak positions across all structures (Figure 6b).

15272648, 2026, 14, Downloaded from https://advanced.onlinelibrary.wiley.com/doi/10.1002/adem.70951 by Spanish Cochrane National Provision (Ministerio de Sanidad), Wiley Online Library on [24/07/2026]. See the Terms and Conditions (https://onlinelibrary.wiley.com/terms-and-conditions) on Wiley Online Library for rules of use; OA articles are governed by the applicable Creative Commons License

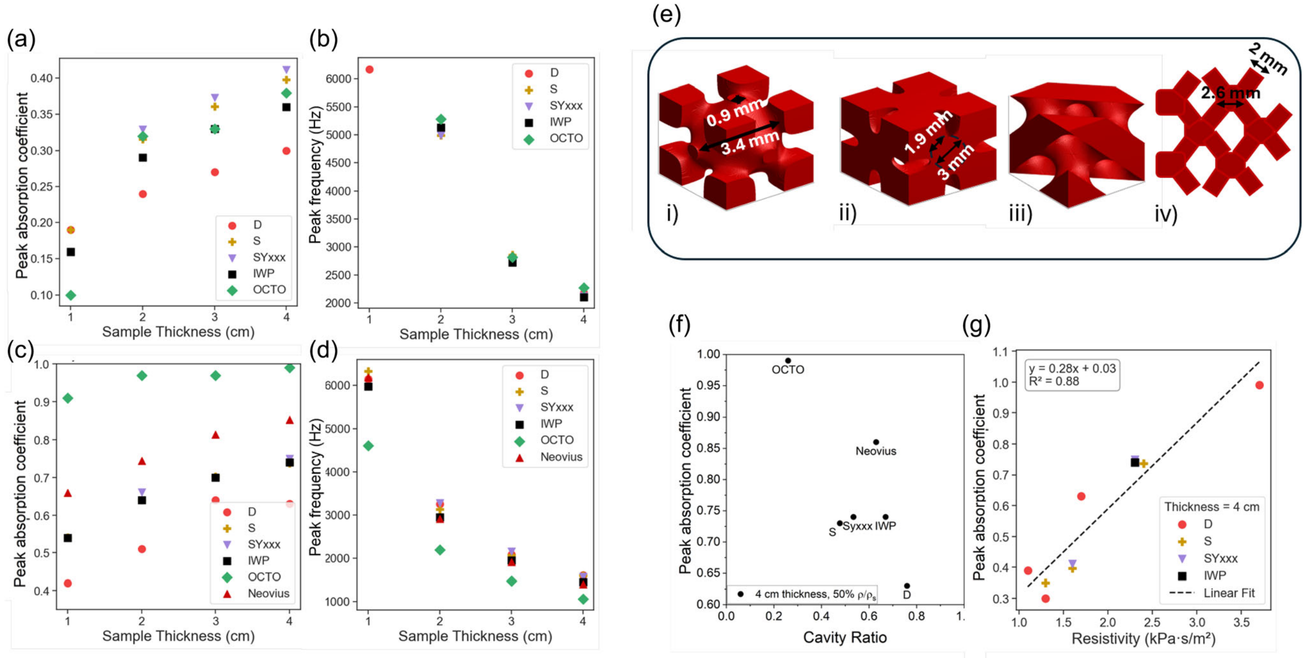

FIGURE 6 | (a) Peak absorption coefficient versus sample thickness and (b) peak absorption frequency versus sample thickness for relative density 25%; (c) peak absorption coefficient versus sample thickness and (d) peak absorption frequency versus sample thickness for relative density 50%; (e) 3D Illustration of the cavities for (i) OCTO, (ii) Neovius, (iii) D, and (iv) 2D representation of D cavity. (f) Peak coefficient of absorption versus cavity ratio for relative density 50% and thickness 4 cm. (g) Peak coefficient of absorption versus flow resistivity for 4 cm sample thickness.

However, architecture does influence the absorption at the resonance peak, with SYxxx (+) exhibiting the highest performance and D (+) the lowest (Figure 6a).

At 50% relative density, the OCTO (+) architecture displays resonance peaks at lower frequencies with markedly higher absorption, significantly outperforming other designs.

Overall, increasing the sample thickness shifts the absorption peak toward lower frequencies, approaching an asymptotic limit. The most significant improvements occur within the 1–4 cm thickness range, with particularly pronounced gains between 3 and 4 cm. Beyond 4 cm, further increases in thickness result in only marginal additional benefits, enabling near-maximal absorption performance within compact dimensions suitable for engineering applications. Measurements performed at a thickness of 5 cm (Figure 5) further confirm the asymptotic behavior.

We next analyze how specific structural and geometrical characteristics of the lattices give rise to the observed acoustic responses. TPMS lattices are inherently wavy, featuring alternating regions of wider and narrower cross sections.

These variations can be qualitatively interpreted as neck–cavity-like features embedded within a continuous and fully interconnected geometry, rather than as discrete Helmholtz resonators with well-defined characteristic dimensions. Figure 6e shows the measurements of the wider and narrower cross sections within the cavity networks, corresponding to the inverse (air-filled) domains of the different TPMS geometries. When applying the classical Helmholtz resonator model [29], including the correction for multiple necks [30] to account for the labyrinthine nature of TPMS structures, the predicted resonance frequencies deviate significantly from the measured values. To better rationalize the results, we computed a cavity ratio, defined as the ratio between the characteristic diameter of the narrower constrictions (neck) and that of the wider cavity regions. Figure 6f demonstrates a clear inverse correlation between absorption coefficient and cavity ratio: architectures with lower cavity ratios, corresponding to stronger geometric constrictions (e.g., OCTO and Neovius), exhibit significantly higher peak absorption coefficients (∼0.9–1.0), whereas architectures with higher cavity ratios, characterized by weaker constrictions (e.g., Diamond and SYxxx), show lower absorption (∼0.4–0.7). This trend highlights that geometric tuning of neck-to-cavity proportions—primarily governed by constriction cross-section—shows a strong correlation with the acoustic performance in the resonance regime at the investigated densities and thicknesses.

In addition to the sound absorption curves, air-flow resistivity was measured for selected architectures and is presented in Table 1. Air-flow resistivity is an intrinsic property of each architecture and relative density, directly related to tortuosity and representing the material's resistance to viscous airflow through its porous network. Although the absorption coefficient varies with sample thickness, air-flow resistivity remains independent of it, serving as a fundamental descriptor of the lattice's dissipative capacity. Notably, Figure 6g reveals a strong positive correlation between air-flow resistivity and peak absorption coefficient: architectures with higher resistivity (S at 2.4 kPa·s/m^2 and SYxxx at 2.3 kPa·s/m^2) exhibit superior absorption performance, while those with lower resistivity (D at 1.1–1.7 kPa·s/m^2) show reduced absorption. This relationship underscores that greater flow resistance enhances viscothermal dissipation at the neck–cavity interfaces, amplifying energy loss mechanisms critical for resonance-dominated absorption in TPMS lattices.

15272648, 2026, 14, Downloaded from https://advanced.onlinelibrary.wiley.com/doi/10.1002/adem.70951 by Spanish Cochrane National Provision (Ministerio de Sanidad), Wiley Online Library on [24/07/2026]. See the Terms and Conditions (https://onlinelibrary.wiley.com/terms-and-conditions) on Wiley Online Library for rules of use; OA articles are governed by the applicable Creative Commons License

TABLE 1 | Measured air flow resistivity.

Architecture	Relative density	Flow resistivity, $kPa \cdot s \cdot m^{-2}$
D (+)	15	1.1
D (+)	25	1.3
D (+)	50	1.7
S (+)	15	1.3
S (+)	25	1.6
S (+)	50	2.4
SYxxx (+)	15	2.2
SYxxx (+)	25	1.6
SYxxx (+)	50	2.3
IWP (+)	50	2.3

2.2.1 | Effect of Density Grading

To further explore the design space covered by TPMS, the effect of density grading on sound absorption was explored. To this end, two architectures where studied: D(+), since its low pinch-off allows for a pronounced density gradient, and OCTO (+), since it exhibits the highest coefficient of absorption. Thus, for D (+) a 4 cm thick sample was designed applying a linear density gradient from 15% to 75% relative density. Sound absorption curves were obtained for both configurations: with the incident wave applied to the low-density face and to the high-density face. A further sample with a V-shaped density gradient was designed, decreasing from 75% to 15% relative density at the midplane and increasing again to 75% at the opposite face.

The sound absorption curve of homogeneous D (+) sample of 75% relative density was additionally measured for completeness of the study and reported in the Supporting Information, Section 0.6, Figure S21. The resulting average density of these to samples was measured as 40%. An homogeneous sample with 40% relative density was produced as benchmark.

In all cases, thickness and average relative density were kept constant, ensuring identical total mass and global dimensions. This mass- and thickness-equivalent comparison isolates the effect of spatial material distribution on acoustic performance while controlling for bulk parameters.

Photographs of the manufactured designs as well as the resulting absorption curves are presented in Figure 7.

All visible features in the structures correspond to the intended lattice design. Based on prior X-ray computed tomography of similar samples manufactured under the same conditions, the internal porosity associated with the FFF process is approximately 1%, which is not expected to affect the acoustic measurements.

It can be seen that graded designs offer clear advantages over nongraded configurations of equivalent thickness and mass.

These differences cannot be attributed to bulk effects, but instead arise from the through-thickness redistribution of material, which modifies the local acoustic impedance profile and wave–structure coupling.

The acoustic response of the graded sample is primarily governed by the region that first interacts with the incident sound wave. When the low-density section faces the incoming wave, the response is broadband, characteristic of porous materials, whereas exposure of

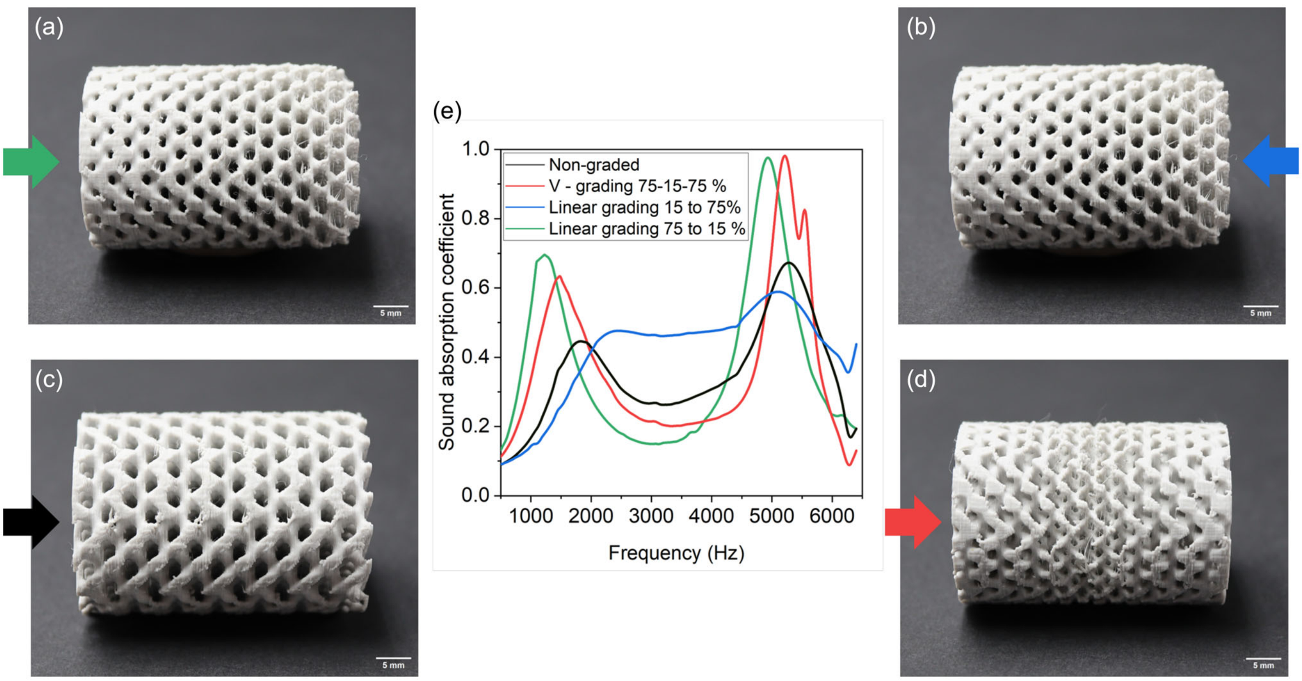

FIGURE 7 | Photographs of manufactured samples (a) linear graded, 75% to 15% relative density; (b) linear graded, 15% to 75% relative density; (c) nongraded, relative density 40%; (d) V-shaped density gradient, 75%–15%–75%; the arrow in each photograph indicates the incident sound wave direction, color coded with the obtained sound absorption curve, plotted in (e).

15272648, 2026, 14, Downloaded from https://advanced.onlinelibrary.wiley.com/doi/10.1002/adem.70951 by Spanish Cochrane National Provision (Ministerio de Sanidad), Wiley Online Library on [24/07/2026]. See the Terms and Conditions (https://onlinelibrary.wiley.com/terms-and-conditions) on Wiley Online Library for rules of use; OA articles are governed by the applicable Creative Commons License

the high-density region results in resonance-dominated behavior with higher absorption coefficients than in the homogeneous case.

For OCTO (+), the applied density gradient was restricted to the range of 25%–50% relative density due to pinch-off constraints. The same gradient patterns applied to D (+) were reproduced for OCTO (+), spanning 25%–50%, 50%–25%, and a V-shaped profile (50%–25%–50%). In all cases, the resulting average relative density was approximately 40%. For benchmarking purposes, a homogeneous nongraded sample with a relative density of 40% was also fabricated and tested. The obtained absorption curves are presented in Figure 8.

While the general trend of higher absorption coefficients when the sound wave impinges on the denser side is maintained, the effect of grading in OCTO (+) is notably more moderate, consistent with its less steep density gradient.

3 | Discussion

3.1 | Mechanical Property Space

In this work, we undertake the broader mechanical property space mapping for strut-based TPMS to date, extending previous uniaxial compression characterization to shear and bulk.

A key outcome of this work is the establishment of a unified mechanical property map that brings together a large set of TPMS architectures and classical truss lattices within a common framework. This mapping approach makes it possible to identify not only absolute performance trends but also relative positioning, tradeoffs, and outliers across fundamentally different architectural families. In this context, stretch-dominated lattices such as the octet define an upper bound in stiffness-to-weight efficiency, while TPMS architectures populate a broader region of the design space characterized by more complex deformation pathways. Importantly, this broader distribution reflects not a deficiency, but an expansion of accessible mechanical responses, which becomes particularly relevant when multifunctional requirements are considered.

The comparison between the proposed experimental shear tests and the numerical simulations indicates that the model captures the overall trends in the elastic response of the lattices across different relative densities. The experimental results exhibit low variability across replicates, supporting the robustness and reproducibility of the proposed methodology for characterizing shear behavior in TPMS architectures. Systematic deviations in magnitude are observed are acknowledged.

The differences in yield behavior can be attributed to both material and testing factors. In particular, interlayer bonding weaknesses and manufacturing-induced defects in the additively manufactured specimens reduce the experimental yield strength. In addition, the stress state in the double-notched configuration deviates from ideal pure shear, resulting in mixed shear–tension conditions that are not captured in the numerical model.

Strikingly, the measured shear moduli deviate from the expected inverse correlation with the Gibson–Ashby exponent n and cannot be rationalized by the LASF alone, revealing the intricate dependence of G on connectivity, cross-sectional heterogeneity, and strain distribution pathways. While a rigorous definition of lattice rigidity would require computation of the equilibrium matrix [31], the nonpolyhedral nature of TPMS prevents an analytical enumeration of beams and nodes, making such a topological assessment

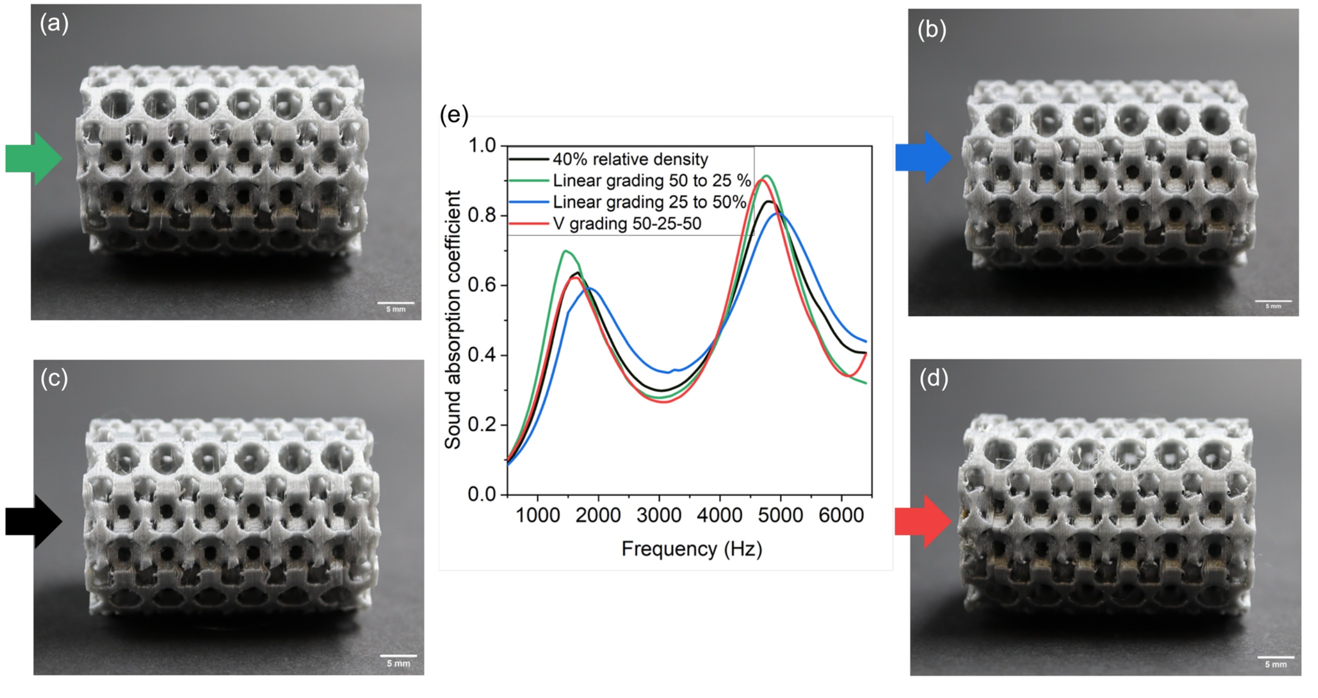

FIGURE 8 | Obtained sound absorption curve for photographs of manufactured samples (a) linear graded, 50% to 25% relative density; (b) linear graded, 25% to 50% relative density; (c) nongraded, relative density 40%; (d) V-shaped density gradient, 50%–25%–50%; the arrow in each photograph indicates the incident sound wave direction, color coded with the obtained sound absorption curve, plotted in (e).

15272648, 2026, 14, Downloaded from https://advanced.onlinelibrary.wiley.com/doi/10.1002/adem.70951 by Spanish Cochrane National Provision (Ministerio de Sanidad), Wiley Online Library on [24/07/2026]. See the Terms and Conditions (https://onlinelibrary.wiley.com/terms-and-conditions) on Wiley Online Library for rules of use; OA articles are governed by the applicable Creative Commons License

impractical. Due to this limitation, we have avoided the term "topology" throughout the manuscript and instead refer to the "architecture" of the TPMS structures.

Importantly, this discrepancy cannot be attributed solely to geometric complexity. In previous work on similar TPMS architectures under compressive loading, both the Gibson–Ashby scaling and LASF have shown good predictive capability, including in bending-dominated regimes [23]. The present results therefore point to a fundamental difference associated with the loading mode. In this context, it is worth noting that shear behavior in architected materials has received comparatively limited attention, and that the Gibson–Ashby model itself was originally developed for compressive loading and only later extended to other loading conditions.

The inability to rigorously compute topological metrics, together with the observation that descriptors such as the LASF or the Gibson–Ashby scaling exponent n fail to consistently predict shear behavior, underscores the complex, high-dimensional parameter space of TPMS architectures. More broadly, these results highlight the practical limits of existing analytical models and simplifying assumptions when applied to shear-dominated deformation and point to the need for the development of predictive frameworks specifically tailored to such loading conditions.

Our results further indicate that, for purely mechanical stiffness at fixed relative density, structural complexity in strut-based TPMS does not necessarily translate into superior performance. Instead, the additional material is often located in regions that remain relatively stress-free under macroscopic loading, making stretch-dominated truss lattices such as the octet the most efficient choice when mechanical rigidity alone is the design target. The real strength of TPMS does not lie in maximizing stiffness alone, but in their ability to simultaneously accommodate mixed and multiaxial stiff–compliant mechanical requirements while enabling additional functionalities, most notably sound absorption.

3.2 | Sound Absorption

From the extensive characterization work undertaken across architectures and relative densities, our work reveals that, for relative densities up to 25%, the absorption frequencies of all architectures collapse onto one common trend. At these low solid fractions, lattices behave as porous media where absorption is dictated solely by relative density, rendering architectural distinctions acoustically irrelevant [32]. As relative density increases, architecture-specific effects emerge, driving a progressive transition from broadband porous absorption to resonant behavior. The absorption coefficient can be enhanced and resonance peak frequency reduced by: (a) increasing relative density, which amplifies viscothermal dissipation in cavity–neck structures; and (b) increasing thickness. Although weight and thickness constrain engineering applications like acoustic liners, the 4 cm thickness falls within a realistic and practically viable range.

As the relative density increases, clear architecture-specific acoustic effects emerge, accompanied by a progressive transition from broadband porous-type absorption to increasingly resonant behavior. While attempts to rationalize the measured absorption peaks using classical Helmholtz resonator models [29]—including extensions accounting for multiple necks [30] and end corrections [33]—were unable to accurately reproduce the measured resonance frequencies without introducing fitting parameters specific to each architecture in predicting the observed resonance frequencies, a clear correlation is nevertheless found between the neck-to-cavity ratio of the investigated architectures and the degree of resonance, manifested by a shift toward lower absorption frequencies and increased peak absorption coefficients as the ratio between the narrower and wider cross sections decreases. It should be emphasized that Helmholtz-type models inherently describe resonance peak frequencies but do not predict absorption amplitudes. In this context, although the sound absorption coefficient systematically increases with sample thickness for all architectures, a pronounced influence of flow resistivity on the absorption coefficient is also observed, indicating that viscothermal dissipation and cavity-driven resonance mechanisms [34, 35] act jointly in governing the acoustic response. The correlation between the absorption value exhibited by the resonance peak and flow resistivity has also been observed in TPMS by previous authors [19]. While these authors use the Johnson–Champoux–Allard (JCA) to model the Gyroid and D behavior, we have refrained to do so since JCA assumes a clear scale separation between the viscous boundary layer thickness and the characteristic pore size—an assumption that does not hold in the architected lattices under study.

While most previous studies have investigated the sound absorption performance of TPMS when used as the core of sandwich structures coupled with perforated panels [4, 36–38], the present results demonstrate that TPMS architectures can achieve high acoustic absorption as standalone elements. This removes the need for additional perforated facings, thereby reducing manufacturing steps and material interfaces and offering a clear advantage in terms of simplified fabrication, reduced material usage, and improved recyclability.

This duality between porous dissipation at low relative densities and neck–cavity–controlled resonance at higher relative densities provides the mechanistic basis for the multifunctional tuning of TPMS absorbers and can be harnessed through density grading of the architectures.

Given that all graded and homogeneous samples share identical thickness and average density, the observed differences arise from the redistribution of local acoustic impedance along the propagation direction rather than from bulk mass effects.

The present results show that the dominant absorption mechanism is primarily dictated by the initial section encountered by the incident sound wave, opening the possibility to substantially reduce the overall weight of the absorber while maintaining high acoustic performance through grading.

Architectures characterized by a highly heterogeneous mass distribution, such as OCTO (+), exhibit systematically lower cavity-to-neck ratios, which promotes stronger resonant effects and leads to higher absorption coefficients. However, this same mass heterogeneity also results in an early pinch-off, as local solid accumulation causes loss of connectivity at lower relative densities.

15272648, 2026, 14, Downloaded from https://advanced.onlinelibrary.wiley.com/doi/10.1002/adem.70951 by Spanish Cochrane National Provision (Ministerio de Sanidad), Wiley Online Library on [24/07/2026]. See the Terms and Conditions (https://onlinelibrary.wiley.com/terms-and-conditions) on Wiley Online Library for rules of use; OA articles are governed by the applicable Creative Commons License

Consequently, such architectures exist only over a narrow density window, which inherently limits their grading potential. This reveals a fundamental trade-off between maximizing resonant absorption through geometric heterogeneity and preserving a sufficiently broad density range for effective functional grading.

Beyond acoustic performance, the weight–sound optimization enabled by density grading can be further coupled with topological optimization of the TPMS architecture to simultaneously tailor the mechanical response for load-bearing multifunctional applications.

4 | Conclusion

In this work, we have established one of the most extensive property–architecture–density design space maps for TPMS lattices reported to date, spanning both mechanical and acoustic absorption functionalities. Beyond providing a broad comparative dataset, this study introduces a novel experimental shear testing methodology specifically tailored for lattice materials, enabling direct access to shear moduli and extending experimental lattice characterization beyond the predominantly uniaxial compression frameworks available in the literature.

From a mechanical standpoint, our results reveal that neither the Gibson–Ashby scaling exponents nor commonly used geometric descriptors such as the LASF provide reliable predictors of bulk or shear rigidity in TPMS architectures despite their previously demonstrated applicability under compressive loading for similar structures.

In particular, the absence of correlation between LASF and shear modulus, as well as between scaling exponents and G and K moduli, highlights the complex and coupled nature of strain distribution, connectivity, and cross-sectional heterogeneity in these structures.

This behavior is further compounded by the comparatively limited attention that shear loading has received in architected materials, where most existing models have been developed and validated primarily under compressive conditions. These findings expose the practical limits of existing analytical and semiempirical models when applied to TPMS-based architectures, particularly under shear loading, which remains comparatively underexplored in lattice materials, and underscore the need for new multiscale descriptors and modeling approaches that explicitly incorporate both architectural complexity and loading-mode dependence. Concerning acoustic performance, we demonstrate that for relative densities below approximately 25%, the absorption frequencies of all investigated architectures collapse onto a single trend, indicating that sound absorption in this regime is governed primarily by porosity and is largely insensitive to architecture. As the relative density increases, a clear transition toward resonance-dominated absorption emerges. Specifically, decreasing cavity-to-neck ratios lead to systematically lower absorption frequencies and increased absorption coefficients, cavity-type resonance governed by the coupled neck–cavity impedance. While classical and adapted Helmholtz resonator models fail to predict the measured absorption frequencies, we identify flow resistivity as a dominant parameter governing the magnitude of sound absorption, confirming the critical role of cavity-driven dissipation. Architectures exhibiting strong mass redistribution and pronounced cross-sectional heterogeneity display enhanced resonant absorption but also suffer from increased pinch-off, restricting their accessible density range and thus limiting their grading potential.

A key outcome of this work is the demonstration that both the dominant absorption mechanism and the overall acoustic performance are strongly dictated by the initial face encountered by the incident sound wave. This enables efficient acoustic tailoring through density grading, particularly for architectures with wide accessible density ranges, allowing substantial weight reduction while preserving high absorption performance. Importantly, this acoustic grading strategy can be directly coupled with topological and architectural optimization of mechanical properties, opening a robust pathway toward genuinely multifunctional, load-bearing acoustic materials.

Taken together, our results demonstrate that the true advantage of TPMS lattices does not lie in the maximization of mechanical rigidity alone—where classical stretch-dominated truss lattices such as the octet remain more weight-efficient—but rather in their exceptional potential for multifunctional integration. By enabling the simultaneous and programmable control of mechanical stiffness, shear response, and sound absorption through architecture, density, and grading, TPMS lattices emerge as a powerful design platform for next-generation multifunctional materials systems.

5 | Experimental Section

5.1 | Computational Modeling of TPMS Elastoplastic Behavior

Representative volume elements (RVEs) of the TPMS families were generated and analyzed using finite element modeling in a cubic domain of edge length L.

The RVE approach assumes periodicity of the underlying architecture and sufficient scale separation between the unit cell and the macroscopic response, such that the mechanical behavior can be represented by a single periodic cell.

Periodic volume meshes were constructed with the Pygalmesh Python interface [39], which is based on the open-source CGAL library [40]. The TPMS structures were described by their implicit equations in either negative ($\phi(\bar{x}, \bar{y}, \bar{z}) - t < 0$) or positive ($\phi(\bar{x}, \bar{y}, \bar{z}) + t > 0$) form. A schematic representation of the generated meshes can be found elsewhere [23]. The level-set parameter t determines the solid fraction and was adjusted to achieve target relative densities ρ/ρ_s. To this end, a Python routine employing the fast-marching method was implemented to generate .stl geometries corresponding to prescribed densities. Finite element discretisation was performed in Abaqus/Standard with C3D10MH elements (10-node modified tetrahedra, hybrid formulation with linear pressure, and hourglass control). The bulk polymer was modeled as an elastic–plastic material, with parameters identified from experiments on printed dense specimens. The elastic constants were measured as $E_s = 1980 \pm 35$ MPa and $\nu_s = 0.3$, while the yield strength was $\sigma_{ys} = 49.0 \pm 0.3$ MPa. Plastic flow was

15272648, 2026, 14, Downloaded from https://advanced.onlinelibrary.wiley.com/doi/10.1002/adem.70951 by Spanish Cochrane National Provision (Ministerio de Sanidad), Wiley Online Library on [24/07/2026]. See the Terms and Conditions (https://onlinelibrary.wiley.com/terms-and-conditions) on Wiley Online Library for rules of use; OA articles are governed by the applicable Creative Commons License

described by J_2 theory with isotropic hardening. Periodic boundary conditions (PBCs) were enforced by pairing opposite nodes on each cuboid face via multipoint constraints in Abaqus, as described in [41, 42]. Stress–strain curves were extracted from the reaction forces and averaged deformation measures following the finite deformation framework. The simulations accounted for elastic–plastic behavior but excluded effects of densification or wall-to-wall contact.

All simulations were conducted on idealized, defect-free geometries derived directly from the implicit TPMS descriptions. Consequently, manufacturing-induced imperfections associated with the additive manufacturing process, such as geometric deviations, surface roughness, or reduced interlayer bonding strength, were not explicitly included in the numerical model.

5.2 | Fabrication and Shear Tests of Selected Geometries

Double-notch shear specimens were designed based on the geometry defined in the ASTM7078 [24] standard for composite materials.

Double-notch shear specimens were designed based on the geometry defined in [20] (ASTM D7078) for composite materials. This standard was developed to improve the uniformity of the shear stress distribution in the gauge section and to reduce parasitic bending effects compared to earlier shear test methods. Accordingly, it is widely adopted for approximating shear-dominated loading conditions in structured materials. While this configuration promotes a relatively uniform shear stress state within the reduced section between the notches, a perfectly uniform state of pure shear is not achieved. Stress gradients persist near the notch roots and free surfaces, and the local stress state may evolve with increasing deformation.

The specimen dimensions were maintained as specified in the standard, while the central notched section was filled with TPMS lattices. The lateral sections, corresponding to the gripping areas, were kept solid to ensure proper load transfer. A unit cell was centered precisely within the middle of the notched region to replicate the stress distribution applied in the numerical simulations. The overall specimen thickness corresponded to two unit cells, ensuring full structural connectivity. The .stl were generated using [43], sliced with Prusa Slicer 2.9.1 and printed in a Prusa i3MK3 printer (Prague, Czech Republic) with Kimya Tough poly lactic acid (PLA)-HI Filament. Shear tests were conducted in an Instron universal testing machine (MA, USA) under 1 mm min^{-1} stroke control. The force was measured with a 3 kN cell. In addition, the local surface deformation was followed using 2D DIC with images acquired with an Allied vision Stingray F504BASG stereocamera (Stadtroda, Germany) at 1 Hz. The full-field shear strain distribution was obtained by image processing with VIC-2D software from Correlated Solutions (South Carolina, USA). The shear strain reported in the stress strain curves was determined by DIC using the open-source μDIC Python framework [44]. A feature-based approach was employed, in which 10 discrete tracking points (five on each side of the notch) were manually selected. The shear strain was calculated from the relative displacement of these points across the notch during loading.

5.3 | Fabrication and Tests with Impedance Tube

Samples of 29 and 100 mm in diameter, with a consistent unit cell length of 5.88 mm, were designed, using [43] software. Preliminary measurements were conducted on samples with different unit cell sizes (2.85, 5.88, and 10 mm). No measurable influence of unit cell size on the sound absorption curves was observed within the investigated range (see Supporting Information, Section 0.4, Figure S19). The .stl files were sliced with Prusa Slicer 2.9.1 and printed in a Prusa i3MK3 printer (Prague, Czech Republic) with Kimya Tough poly lactic acid (PLA)-HI Filament. The sound absorption coefficient described in this study was measured in an impedance tube following the two microphones transfer function method standardized in ISO 10534-2:2023 [45]. The system measures the complex transfer function, H_{12}, between two microphones, 1 and 2, positioned in front of the material being tested based on their pressure readings [46]. This transfer function encodes information about both the amplitude and phase of the sound wave at each microphone position, arising from the superposition of the forward-traveling (incident) and backward-traveling (reflected) waves. The normal incidence reflection coefficient r at the surface of the test sample is calculated form the transfer function using the formula:

$$r = \frac{H_{12} e^{-jks_1} - e^{-jks_2}}{e^{jks_2} - H_{12} e^{jks_1}}$$

where H_{12} is the measured transfer function between the two microphones, k is the complex wave number, and s_1 and s_2 represent the distances from the respective microphones to the surface of the sample. The absorption coefficient is subsequently calculated as $\alpha = 1 - |r|^2$. A Model 4206 Bruel and Kjaer impedance tube was used with two Model 4186 Bruel and Kjaer microphones. A 3560 C Pulse Analyzer was used to process the signal using the Material Testing software. The excitation signal at the impedance tube, a broadband noise covering the frequencies of interest, was generated using a Pioneer A-305 R amplifier in conjunction with the Pulse Analyzer. For measurements in the low-frequency range (100–1600 Hz), a tube with a larger diameter (100 mm) is used, whereas higher frequencies (500–6400 Hz) are measured using a tube of smaller diameter (29 mm). The sound absorption coefficient measured is the average of the measurement of three samples of the same characteristics. In order to check reproducibility, all measurements were performed on two different days. Throughout the testing, the samples were installed with their surfaces directly against the rigid back plate of the impedance tube.

5.4 | Flow Resistivity

The static airflow resistivity σ of the samples was measured using an experimental device designed in UPM acoustics laboratory in accordance with ISO 9053-1:2018 [47]. The apparatus consists of an air supply system, a flow meter, and a digital manometer with a resolution of 0.1 Pa, which records the pressure drop across the sample. Once the airflow through the porous specimen stabilizes

15272648, 2026, 14, Downloaded from https://advanced.onlinelibrary.wiley.com/doi/10.1002/adem.70951 by Spanish Cochrane National Provision (Ministerio de Sanidad), Wiley Online Library on [24/07/2026]. See the Terms and Conditions (https://onlinelibrary.wiley.com/terms-and-conditions) on Wiley Online Library for rules of use; OA articles are governed by the applicable Creative Commons License

and becomes steady, the pressure difference is measured as a function of the flow rate.

To ensure accurate and reliable measurements, the airflow through the sample must remain laminar since turbulence can introduce nonlinearities and distort the results. Under laminar flow conditions, the static airflow resistivity σ is calculated using

$$\sigma = \frac{\Delta P}{F}\frac{S}{d}$$

where ΔP is the pressure drop across the sample, F is the volumetric flow rate of air, and S and d are the cross-sectional area and thickness of the sample, respectively.

To further verify laminar flow and reduce measurement uncertainty, multiple readings were taken at different flow rates for each specimen. The ratio $\Delta P/F$ was determined as the slope of a linear regression of the measured pressure drops ΔP versus the flow rates F. The samples with diameter of 100 mm were used.

Acknowledgments

This project received funding from the European Union's Horizon 2020 research and innovation program under the Marie Skłodowska Curie grant agreement no. 101106955. Support by Jose Luís Jimenez, Vanesa Martinez, and Macéo Milanesi-Giraudo with the shear experiments is gratefully acknowledged. L.D. would like to thank Jingyi Zhang for valuable discussions.

Funding

This work was supported by H2020 Marie Skłodowska-Curie Actions (101106955).

Conflicts of Interest

The authors declare no conflicts of interest.

Data Availability Statement

The data that support the findings of this study are available in the Supporting Information of this article.

References

1. Z. Li, X. Wang, Z. Wang, et al., "Emerging Acousto-Mechanical Metamaterials: From Physics-Guided Design to Coupling-Driven Performance," *Materials Today* 89 (2025): 151–171, https://doi.org/10.1016/j.mattod.2025.06.029.

2. Z. Li, X. Li, Z. Wang, and W. Zhai, "Multifunctional Sound-Absorbing and Mechanical Metamaterials via a Decoupled Mechanism Design Approach," *Materials Horizons* 10 (2023): 75–87, https://doi.org/10.1039/D2MH00977C.

3. Z. Li, K. Zeng, Z. Guo, et al., "All-in-One: An Interwoven Dual-Phase Strategy for Acousto-Mechanical Multifunctionality in Microlattice Metamaterials," *Advanced Functional Materials* 35, no. 20 (2025): 2420207, https://doi.org/10.1002/adfm.202420207.

4. Z. Li, Y. Zhou, X. Kong, et al., "Sound Absorption Performance of a Micro-Perforated Plate Sandwich Structure Based on Selective Laser Melting," *Virtual and Physical Prototyping* 19, no. 1 (2024): e2321607, https://doi.org/10.1080/17452759.2024.2321607.

5. A. H. Schoen, *Infinite Periodic Minimal Surfaces without Self-Intersections: Three Dimensional Euclidean Space Partitioned into Interpenetrating Labyrinths by Infinite Periodic Minimal Surfaces without Self Intersections*, https://ntrs.nasa.gov/citations/19700020472.

6. R. Nesper and H.-G. von Schnering, "Periodic Potential Surfaces in Crystal Structures," *Angewandte Chemie, International Edition in English* 25, no. 1 (1986): 110–112, https://doi.org/10.1002/anie.198601101.

7. H. G. von Schnering and R. Nesper, "Nodal Surfaces of Fourier Series: Fundamental Invariants of Structured Matter," *Zeitschrift für Physik B Condensed Matter* 83, no. 3 (1991): 407–412, https://doi.org/10.1007/BF01313411.

8. M. Wohlgemuth, N. Yufa, J. Hoffman, and E. L. Thomas, "Triply Periodic Bicontinuous Cubic Microdomain Morphologies by Symmetries," *Macromolecules* 34, no. 17 (2001): 6083–6089, https://doi.org/10.1021/ma0019499.

9. J. W. Fisher, S. W. Miller, J. Bartolai, T. W. Simpson, and M. A. Yukish, "Catalog of Triply Periodic Minimal Surfaces, Equation-Based Lattice Structures, and Their Homogenized Property Data," *Data in Brief* 49 (2023): 109311, https://doi.org/10.1016/j.dib.2023.109311.

10. S. Torquato, S. Hyun, and A. Donev, "Multifunctional Composites: Optimizing Microstructures for Simultaneous Transport of Heat and Electricity," *Physical Review Letters* 89, no. 26 (2002): 266601, https://doi.org/10.1103/PhysRevLett.89.266601.

11. S. N. Khaderi, V. S. Deshpande, and N. A. Fleck, "The Stiffness and Strength of the Gyroid Lattice," *International Journal of Solids and Structures* 51, no. 23-24 (2014): 3866–3877, https://doi.org/10.1016/j.ijsolstr.2014.06.024.

12. A. S. Dalaq, D. W. Abueidda, and R. K. Abu Al-Rub, "Mechanical Properties of 3D Printed Interpenetrating Phase Composites with Novel Architectured 3D Solid-Sheet Reinforcements," *Composites Part A: Applied Science and Manufacturing* 84 (2016): 266–280, https://doi.org/10.1016/j.compositesa.2016.02.009.

13. I. Maskery, L. Sturm, A. O. Aremu, et al., "Insights into the Mechanical Properties of Several Triply Periodic Minimal Surface Lattice Structures Made by Polymer Additive Manufacturing," *Polymer* 152 (2018): 62–71, https://doi.org/10.1016/j.polymer.2017.11.049.

14. M. Alizadeh-Osgouei, Y. Li, A. Vahid, A. Ataee, and C. Wen, "High Strength Porous PLA Gyroid Scaffolds Manufactured via Fused Deposition Modeling for Tissue-Engineering Applications," *Smart Materials in Medicine* 2 (2021): 15–25, https://doi.org/10.1016/j.smaim.2020.10.003.

15. S. M. Sajadi, P. S. Owuor, S. Schara, et al., "Multiscale Geometric Design Principles Applied to 3D Printed Schwarzites," *Advanced Materials* 30, no. 1 (2018): 1704820, https://doi.org/10.1002/adma.201704820.

16. M. Afshar, A. P. Anaraki, H. Montazerian, and J. Kadkhodapour, "Additive Manufacturing and Mechanical Characterization of Graded Porosity Scaffolds Designed Based on Triply Periodic Minimal Surface Architectures," *Journal of the Mechanical Behavior of Biomedical Materials* 62 (2016): 481–494, https://doi.org/10.1016/j.jmbbm.2016.05.027.

17. G. K. Maharjan, S. Z. Khan, S. H. Riza, and S. H. Masood, "Compressive Behaviour of 3D Printed Polymeric Gyroid Cellular Lattice Structure," *IOP Conference Series: Materials Science and Engineering* 455, no. 1 (2018): 012047, https://doi.org/10.1088/1757-899X/455/1/012047.

18. K. Xiang-nan, L. Bin, L. Zhong-Hua, Z. Peng-Fei, and S. Chao, "Research on Sound Absorption Properties of Tri-Periodic Minimal Surface Sandwich Structure of Selective Laser Melting Titanium Alloy," *MATERIALS TRANSACTIONS* 64, no. 4 (2023): 861–868, https://doi.org/10.2320/matertrans.MT-M2022164.

19. J. Godakawela, A. Lomte, and B. Sharma, "Sound Absorption in Uniform and Layered Gyroid and Diamond Triply Periodic Minimal Surface Porous Absorbers," *Applied Acoustics* 236 (2025): 110761, https://doi.org/10.1016/j.apacoust.2025.110761.

20. D. W. Abueidda, I. Jasiuk, and N. A. Sobh, "Acoustic Band Gaps and Elastic Stiffness of Pmma Cellular Solids Based on Triply Periodic Minimal Surfaces," *Materials & Design* 145 (2018): 20–27, https://doi.org/10.1016/j.matdes.2018.02.032.

15272648, 2026, 14, Downloaded from https://advanced.onlinelibrary.wiley.com/doi/10.1002/adem.70951 by Spanish Cochrane National Provision (Ministerio de Sanidad), Wiley Online Library on [24/07/2026]. See the Terms and Conditions (https://onlinelibrary.wiley.com/terms-and-conditions) on Wiley Online Library for rules of use; OA articles are governed by the applicable Creative Commons License

21. T. Silva, J.-Y. Lu, R. K. Abu Al-Rub, and D.-W. Lee, "Investigation on Tailoring the Width and Central Frequency of Bandgaps of Tpms Structures," *International Journal of Mechanics and Materials in Design* 20, no. 2 (2024): 317–1329, https://doi.org/10.1007/s10999-023-09677-2.

22. G. Chouhan, P. Bidare, and G. Bala Murali, "Triply Periodic Minimal Surface Based Lattices for Acoustic Performance," *Noise & Vibration Worldwide* 55, no. 8 (2024): 454–468, https://doi.org/10.1177/09574565241270201.

23. L. Doyle, H. Terrones, and C. González, "On the Rigidity and Mechanical Behavior of Triply Periodic Minimal Surfaces-Based Lattices: Insights from Extensive Experiments and Simulations," *Advanced Engineering Materials* 27 (2025): 2402495, https://doi.org/10.1002/adem.202402495.

24. ASTM D7078/D7078M-20e1, "Standard Test Method for Shear Properties of Composite Materials by V-Notched Rail Shear Method," Developed by subcommitee D30. https://doi.org/10.1520/D7078_D7078M-20E01.

25. L. J. Gibson and M. F. Ashby, *Cellular Solids* (Cambridge University Press, 2014), ISBN 9780521499118, https://doi.org/10.1017/CBO9781139878326.

26. L. Doyle, J. García-Molleja, and C. González, "Low-Velocity Penetration Impact Behavior of Triply Periodic Minimal Surface Strut-Based Lattices," *Advanced Engineering Materials* 27, no. 10 (2025): 2402999, https://doi.org/10.1002/adem.202402999.

27. D. A. Bies, and C. H. Hansen, "Flow Resistance Information for Acoustical Design," *Applied Acoustics* 13, no. 5 (1980): 357–391, https://doi.org/10.1016/0003-682X(80)90002-X.

28. T. J. Cox and P. D'Antonio, *Acoustic Absorbers and Diffusers: Theory, Design and Application*, 3rd ed., ed. T. J. Cox and P. D'Antonio (CRC Press, Taylor & Francis Group, 2017), ISBN 1498740995.

29. A. I. Komkin, M. A. Mironov, and A. I. Bykov, "Sound Absorption by a Helmholtz Resonator," *Acoustical Physics* 63, no. 4 (2017): 385–392, https://doi.org/10.1134/S1063771017030071.

30. N. M. Papadakis, and G. E. Stavroulakis, "Tunable Helmholtz Resonators Using Multiple Necks," *Micromachines* 14, no. 10 (2023): 1932, https://doi.org/10.3390/mi14101932.

31. S. Pellegrino and C. R. Calladine, "Matrix Analysis of Statically and Kinematically Indeterminate Frameworks," *International Journal of Solids and Structures* 22, no. 4 (1986): 409–428, https://doi.org/10.1016/0020-7683(86)90014-4.

32. X. Li, J. W. Chua, X. Yu, et al., "3D-Printed Lattice Structures for Sound Absorption: Current Progress, Mechanisms and Models, Structural-Property Relationships, and Future Outlook," *Advanced Science* 11 (2024): 2305232, https://doi.org/10.1002/advs.202305232.

33. U. Ingard, "On the Design of Acoustic Resonators," *Journal of the Acoustical Society of America* 25, no. 4_Supplement (1953): 830–830, https://doi.org/10.1121/1.1917710.

34. C. R. Liu, J. H. Wu, K. Lu, Z. T. Zhao, and Z. Huang, "Acoustical Siphon Effect for Reducing the Thickness in Membrane-Type Metamaterials with Low-Frequency Broadband Absorption," *Applied Acoustics* 148 (2019): 1–8, https://doi.org/10.1016/j.apacoust.2018.12.008.

35. X. Li, X. Yu, and W. Zhai, "Less Is More: Hollow-Truss Microlattice Metamaterials with Dual Sound Dissipation Mechanisms and Enhanced Broadband Sound Absorption," *Small* 18, no. 44 (2022): e2204145, https://doi.org/10.1002/smll.202204145.

36. P.-F. Zhang, Z.-H. Li, Y.-J. Zhou, et al., "Improved Sound Absorption with 3D-Printed Micro-Perforated Sandwich Structures," *Journal of Materials Research and Technology* 34 (2025): 855–865, https://doi.org/10.1016/j.jmrt.2024.12.082.

37. L. Jian, J. He, G. Wen, Z.-P. Wang, J. Yang, Y. M. Xie, and J. Liu, "*Multifunctional Tpms-Based Metastructures With Enhanced Low-Frequency Sound Absorption and High Bending Stiffness Performance*" (2025), https://doi.org/10.2139/ssrn.5109242.

38. M. Zhang, C. Liu, M. Deng, Y. Li, J. Li, and D. Wang, "Graded Minimal Surface Structures with High Specific Strength for Broadband Sound Absorption Produced by Laser Powder Bed Fusion," *Coatings* 13, no. 11 (2023): 1950, https://doi.org/10.3390/coatings13111950.

39. N. Schlömer, "pygalmesh: Python Interface for CGAL's Meshing Tools," https://github.com/nschloe/pygalmesh.

40. M. Bogdanov, A. Pellé, M. Rouxel-Labbé, and M. Teillaud, "3D Periodic Mesh Generation," in *CGAL User and Reference Manual*, 5.6.1 ed. (CGAL Editorial Board, 2024), https://doc.cgal.org/5.6.1/Manual/packages.html#PkgPeriodic3Mesh3.

41. M. Herráez, C. González, C. S. Lopes, et al., "Computational Micromechanics Evaluation of the Effect of Fibre Shape on the Transverse Strength of Unidirectional Composites: An Approach to Virtual Materials Design," *Composites Part A: Applied Science and Manufacturing* 91 (2016): 484–492, https://doi.org/10.1016/j.compositesa.2016.02.026.

42. M. Herráez, J. Segurado, C. González, and C. S. Lopes, "A Microstructures Generation Tool for Virtual Ply Property Screening of Hybrid Composites with High Volume Fractions of Non-Circular Fibers—VIPER," *Composites Part A: Applied Science and Manufacturing* 129 (2020): 105691, https://doi.org/10.1016/j.compositesa.2019.105691.

43. I. Maskery, L. A. Parry, D. Padrão, R. J. M. Hague, and I. A. Ashcroft, "FLatt Pack: A Research-Focussed Lattice Design Program," *Additive Manufacturing* 49 (2022): 102510, https://doi.org/10.1016/j.addma.2021.102510.

44. S. Olufsen and M. E. Andersen, *μdic: A python Framework for Digital Image Correlation* (Open-source software, MIT License, 2024), https://mudic.readthedocs.io/en/latest/.

45. ISO 10534-2:2023, *Acoustics—Determination of Acoustic Properties in Impedance Tubes: Part 2: Two-Microphone Technique for Normal Sound Absorption Coefficient and Normal Surface Impedance, 2023-10*, https://www.iso.org/standard/81294.html.

46. A. F. Seybert and D. F. Ross, "Experimental Determination of Acoustic Properties Using a Two-Microphone Random-Excitation Technique," *Journal of the Acoustical Society of America* 61, no. 5 (1977): 1362–1370, https://doi.org/10.1121/1.381403.

47. ISO 9053-1: 2018, "Acoustics," Determinatiion of Airflow Resistance. Part 1:Static Airflow Method

Supporting Information

Additional supporting information can be found online in the Supporting Information section.

15272648, 2026, 14, Downloaded from https://advanced.onlinelibrary.wiley.com/doi/10.1002/adem.70951 by Spanish Cochrane National Provision (Ministerio de Sanidad), Wiley Online Library on [24/07/2026]. See the Terms and Conditions (https://onlinelibrary.wiley.com/terms-and-conditions) on Wiley Online Library for rules of use; OA articles are governed by the applicable Creative Commons License